Coded wavefront sensing for video-rate quantitative phase imaging and tomography: validation with digital holographic microscopy

SYED MUHAMMAD KAZIM,[1,*] FRANZISKA STRASSER,[2] MIA KVÅLE LØVMO,[2] ANDRII NEHRYCH,[1] SIMON MOSER,[2] MICHAŁ ZIEMCZONOK,[3] WOLFGANG HEIDRICH,[4] IVO IHRKE,[1] AND MONIKA RITSCH-MARTE[2]

[1] *Zentrum für Sensorsysteme, University of Siegen, Paul-Bonatz-Str. 9-11, 57076 Siegen, Germany*
[2] *Institute of Biomedical Physics, Medical University of Innsbruck , Müllerstr. 44, 6020 Innsbruck, Austria*
[3] *Warsaw University of Technology, Institute of Micromechanics and Photonics, św. Andrzeja Boboli 8, 02-525 Warsaw, Poland*
[4] *Visual Computing Center, King Abdullah University of Science and Technology, Building 1 (Al Khwarizmi) West, Level 2, Thuwal 23955-6900, Saudi Arabia*
[*] *syed.kazim@uni-siegen.de*

Abstract: We demonstrate coded wavefront sensing (Coded WFS) for video-rate quantitative phase imaging and 3D refractive index (RI) tomography of biological specimens. To evaluate the accuracy, we implement an experimental setup that supports measurements of specimens with Coded WFS as well as with digital holographic microscopy (DHM) under identical conditions, enabling direct comparison. We image a static 3D phantom fabricated via additive manufacturing and a rotating HEK293 cell in an acoustofluidic chamber. Our results demonstrate good agreement between the two methods, with the advantage that, in contrast to DHM, Coded WFS enables simple integration with standard microscopes. Furthermore, we apply a standard tomographic reconstruction algorithm to the HEK293 cell data for comparison, which demonstrates the potential of Coded WFS in tomography.

1. Introduction

The volumetric distribution of the refractive index (RI) in cells is linked to biologically relevant structures in their interior [1]. RI tomography enables the recovery of volumetric RI distributions in inhomogeneous specimens such as biological cells, enabling a quantitative characterization of their morphology. It holds great potential for a non-invasive and quantitative study of intracellular matter as it utilizes the intrinsic phase contrast without the need for staining and genetic modifications to create fluorescent markers [2–4].

RI tomography is based on i) quantitative phase imaging (QPI) techniques that enable the label-free imaging of phase specimens and ii) a set of measurements under varying illumination and/or viewing conditions:

i) Digital holographic microscopy (DHM) [5–7] is the gold standard of QPI as it provides reliable, high-resolution access to the complex wavefields. QPI methods can be grouped into two categories: *Single-shot QPI-capable methods*, for example, those that record interferograms, such as DHM, and *computational methods* that record the intensity two or more times, usually at different focus planes, including transport of intensity-based methods [8–10], using optimization algorithms to recover the quantitative phase. The latter group is inherently challenging for snapshot QPI. Even though coded wavefront sensing (Coded WFS) belongs to this category, the reference image can be taken offline and it is, therefore, snapshot-capable. The use of QPI to measure the scattering properties of cells and tissues has been extensively reviewed in [11–13].

ii) The required actuation of the specimens can be achieved by mechanical confinement to a tip or in a capillary attached to a rotation stage [14]. Alternatively, contactless manipulation is a promising research avenue, that has, e.g., been achieved by using optical tweezers to rotate suspended biological cells [15]. Optical trapping for the manipulation of arbitrarily shaped specimens without prior geometric information has also been successfully demonstrated [16]. Acoustic forces have also been used to position and rotate a suspended specimen [17–19]. An alternative method is to provide angled illumination to a static specimen [20, 21]. However, this setup generally suffers from the missing cone problem as the range of angles is smaller. For QPI-based tomography, retrieved complex wavefields from multiple viewing directions have been combined to yield volumetric RI distribution [14–17, 20–23].

In this paper, we propose Coded WFS [24] as a promising candidate for QPI-based 3D RI tomography due to its affordability, single-shot capability, and seamless integration with standard microscopes. We integrate an acoustofluidic device [19] in our setup, enabling specimen rotation and contactless measurements from a full 360° range of viewing angles. This setup fully leverages the benefits of QPI while simultaneously reducing the hardware overhead associated with interferometric methods. In the following, we review both DHM and Coded WFS, as well as RI tomography.

Holographic Microscopy. DHM is an established interferometry-based snapshot QPI method, which inherently offers support for video-rate phase imaging [25, 26]. Gabor originally introduced holographic imaging in an attempt to improve the resolution in electron microscopy [27, 28]. The field of digital holography was only later developed, distinguishing itself from holographic imaging in that it recorded the hologram electronically and not on film [29]. DHM is the application of digital holography to microscopic imaging and has found widespread application in this area due to its ability to measure the phase contrast of objects with high precision [25, 26, 30, 31].

In off-axis DHM, the interference of the object wave with a tilted plane wave ensures that the amplitude and phase of the specimen can be encapsulated within a single intensity image. DHM retrieves the propagated phase of the specimen in the image plane, which is then digitally propagated back to the object plane [5]. The retrieved quantitative phase measures the optical path difference of the specimen along a single axis.

Digital holography remains an active research field for microscopy, tomography, cell identification, and more, as is comprehensively explored in [32]. Moreover, the high accuracy of the recovered phase maps has made DHM the default choice to not only benchmark the performance of other QPI methods but also to evaluate the quality of fabrication processes of sub-micrometer 3D phantoms [33–35].

However, DHM requires careful setup and dedicated hardware for its realization, including damped optical tables and lasers, which makes integration with other optical systems challenging. For more extended 3-dimensional objects, undoing phase wrapping, which occurs when the optical path difference (OPD) exceeds the illumination wavelength, requires additional consideration.

Coded Wavefront Sensing. Another class of QPI methods includes wavefront sensors operating on the same principle as the Hartmann test, which treats the specimen wavefront as transverse aberrations compared to an ideal wavefront [36]. The Hartmann sensor involves an array of apertures a short distance away from the image plane and tracks the motion of diffraction spots relative to their ideal positions due to a non-ideal wavefront and integrates the resulting vector field to retrieve the phase of the specimen.

The aperture array is replaced with a lenslet array to improve the light efficiency in the Shack-Hartmann wavefront sensor (SHWS) [37]. The size of the lenslets has also been reduced to increase the spatial resolution of the SHWS [38]. However, as a consequence, the range of movement for the diffraction spots that can be tracked unambiguously, corresponding to the lenslet size, also reduces. Smaller regions restrict SHWSs to the measurement of small distortions. SHWSs are, therefore, limited by a fundamental trade-off.

It is possible to replace the lenslet arrangement with a thin diffuser or a random phase mask [39–42]. This changes the reference image from a regular grid of spots to a random speckle pattern and enables continuous tracking of the resulting deformation of the speckle grains. We refer to these QPI methods as coded wavefront sensing [42].

Coded WFS requires a reference-specimen pair of intensity images, where the reference is measured only once for an optical setup. The reference speckle pattern is the diffraction pattern of the phase mask, recorded in the absence of a specimen. A second speckle pattern is recorded after inserting the specimen in the optical system. Coded WFS leverages a useful phenomenon known as the optical memory effect [43–45], which relates local tips or tilts in the wavefront incident on the phase mask with local shifts in the reference. In Coded WFS, the motion of the pixels between the reference-specimen pair provides information about the gradient of the phase of the specimen. Optical flow-inspired [46] methods are used to track the motion, which is integrated to obtain the quantitative phase of the specimen.

More recently, algorithmic advancements in Coded WFS have allowed the simultaneous recovery of amplitude and phase of weakly absorbing phase objects [24]. Like DHM, Coded WFS is a snapshot method that allows QPI at video rates. However, Coded WFS is readily integrable with bright-field microscopes, leading to less stringent hardware requirements and a higher potential of being implemented in standard laboratories.

Refractive Index Tomography. Given several input phase maps under different known incident illumination and/or observation directions, the 3D RI distribution of a specimen may be determined in a process known as optical diffraction tomography first described by Wolf [47, 48]. It is based on the Fourier diffraction theorem (FDT) [49, 50] which states that, in the case of weakly scattering objects, the Fourier transform of the field is related to a hemispherical surface in the Fourier transform of scattering potential of the specimen. First practical demonstrations of RI tomography on biological samples were implemented using DHM [14] and utilized optical projection tomography which can be used in conditions where the scattering angles are sufficiently small to enable the use of the Fourier slice theorem (FST) instead of the FDT [21, 22]. Joint absorption and RI tomography based on mechanical scanning of the specimen has been described earlier in [51]. Recent developments include combinations with structured illumination [3], and deconvolution-based recovery from focal stacks [4]. Improved forward models can extend the range of the scattering regime beyond the Born approximation [52–55].

Overview. In Sec. 2, we briefly review the QPI techniques DHM and Coded WFS, where DHM is used as a gold standard to validate Coded WFS as a technique for snapshot QPI, as well as the acoustofluidic trapping device which is fundamental for our dynamic QPI experiments that serve as 3D RI tomography inputs. We provide the details of the experimental setup in Sect. 3.1, which enables imaging the specimen in an identical setting by both methods. We validate the QPI accuracies in Sect. 3.2 by imaging a phantom with a known design OPD: a 3D-printed cluster of objects resembling HeLA cells. We then showcase their video capabilities in Sect. 3.3 by performing video-rate QPI on a real rotating HEK293 cell, where the sustained and periodic rotation of the cell in the acoustofluidic device enables a fair comparison. In Sect. 3.4, we estimate the 3D RI distribution of the HEK cell. We provide a discussion and draw conclusions in Sect. 4.

2. Methods

2.1. Digital Holographic Microscopy

In standard off-axis digital holography, coherent plane wave illumination is split into an object beam that is modulated by the specimen and a reference beam that is tilted by a mirror. The wave fields are combined and measured in the sensor plane. The interference of the object beam with a tilted plane wave ensures that the spectrum of the measurement contains an easily separable propagated transfer function of the unknown specimen, where the separation is governed by the amount of reference beam tilt. Off-axis DHM has been comprehensively developed and analyzed in [6, 7, 56, 57].

DHM offers dependable snapshot QPI capabilities, which has also been leveraged to benchmark the performance of newly developed methods [33, 34]. In this paper, we use a common-path shearing interferometer inspired by [6], tailored for use with the acoustofluidic device. Instead of using a pinhole to generate the reference wave, this DHM variant introduces a spatial shift on the (unfiltered) reference wave, such that a flat part of the beam is overlapped with the location of the object at an angle in the sensor plane. This necessitates that the sample is sparsely distributed, which is fulfilled in our case due to the nodes in the acoustic trapping potential. This precludes the need to consider path matching inside the microscope. The schematic of the setup is shown in Fig. 1 **a**.

2.2. Coded Wavefront Sensing

In Coded WFS, a random phase mask that modulates the phase of the incident wave is placed in close proximity (≈ 1 mm) to the camera sensor. In the absence of the specimen, plane wave illumination generates a speckle pattern in the image plane, which serves as the reference image, $I_0(r)$, for the setup. Subsequently, the unknown phase specimen, $e^{i\phi(r)}$, is inserted in the object plane of the optical setup. The modified speckle pattern in the image plane is measured and is referred to as the object image, $I(r)$.

The relation between $I_0(r)$ and $I(r)$ is estimated by leveraging the optical memory effect [43,44], using the fact that the local changes in the speckle pattern, measured by the apparent flow of the pixels $u(r)$, are proportional to the gradient of the phase of the unknown specimen,

$$u(r) = \frac{z}{k}\nabla\phi(r), \tag{1}$$

where, z is the optical distance between the mask and the sensor determined in a calibration step [24], $k = \frac{2\pi}{\lambda_0}$ is the wavenumber and λ_0 is the illumination wavelength in vacuum. Consequently, the measurements can be written as,

$$I(r) = I_0(r - u(r)), \tag{2}$$

which simplifies wavefront sensing to an optical flow optimization problem [46] to estimate $u(r)$. Either $u(r)$ can be first estimated and then integrated to retrieve the OPD [41, 58], or an optimization strategy can be devised to estimate the OPD from $I(r)$ and I_0 in a single step as proposed in [42].

In this paper, we use the formulation in [24], which allows the unwrapped phase estimation of specimens with weak absorption while also providing the speckle-free bright-field amplitude of the specimen. Moreover, as Coded WFS has been shown to work well with broadband (or white-light) illumination [24, 41], we integrate a white-light illumination unit in the combined experimental setup in Sect. 3.1.

2.3. Acoustofluidic Trapping Device

To image trapped and rotating single cells, we employ an acoustofluidic platform developed in [19] shown in Fig. 1 **b**. The device is tailored for transmission imaging and mounted on an inverted light microscope. Bulk acoustic waves are generated by three lithium niobate ($LiNbO_3$) transducers coupled to a fluid-filled chamber to generate standing waves in three orthogonal directions. The sample is introduced via microfluidic channels into the middle of the chamber where all three acoustic waves intersect. The optically transparent vertical transducer levitates the sample and grants optical access for illumination. The channels are milled in an aluminum carrier and the bottom of the chamber is sealed with a cover slip acting as a reflector for the vertical sound waves and ensuring imaging compatibility. By tuning the relative amplitudes of the three acoustic waves we control the trapping in 3D and the sample orientation. To induce

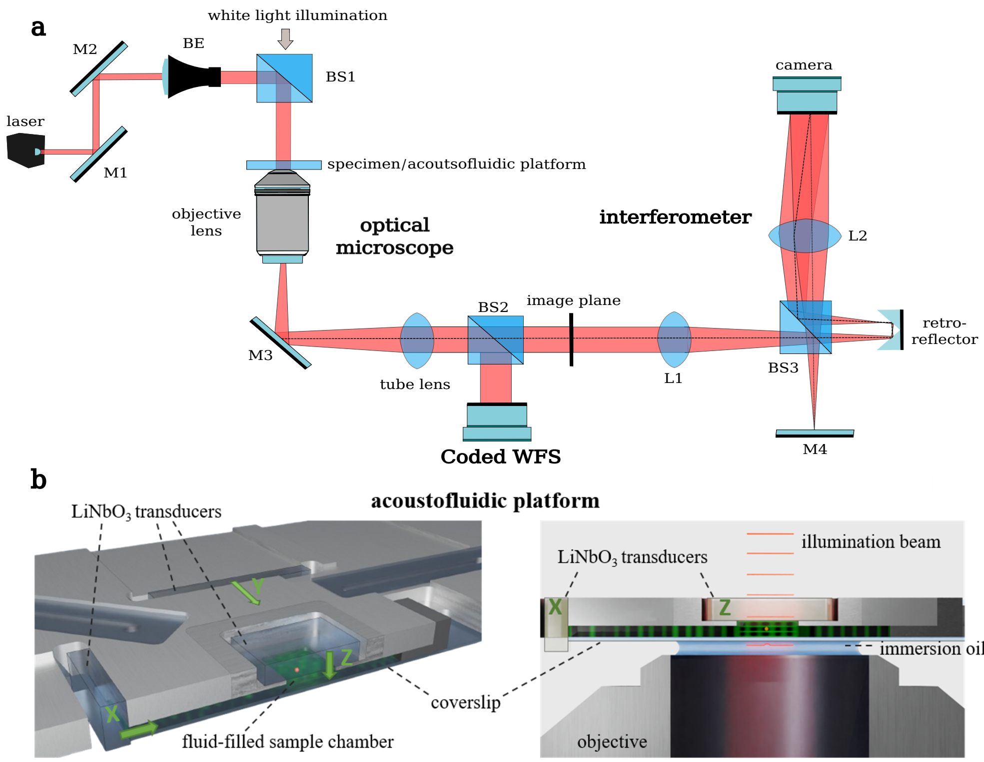

Fig. 1. **a** Experimental setup. The sample is mounted on a commercial inverted microscope (Nikon ECLIPSE Ti2-E) and separately illuminated by two sources: A fibre-coupled diode laser for DHM and a broadband LED for Coded WFS. The scattered light by the specimens is collected using a water immersion objective (1.15 NA, 40x), and two output ports of the microscope are operated sequentially for dynamic measurements. M, mirror; BE, beam expander; BS, beam splitter; L, lens. **b** Acoustofluidic platform. Schematics of the acoustofluidic platform with an angled top view and a cross-section. The propagation direction of the ultrasound from the three orthogonal $LiNbO_3$ transducers in x-, y- and z-direction are indicated with green arrows.

sustained rotations of the sample around an axis orthogonal to the imaging axis, we tune the relative phase and amplitude of the vertical and one horizontal transducer driven at the same frequency (5th harmonic frequency around 20 MHz). The rotating sample maintains rotation periodicty, ensuring comparable successive revolutions. To record the specific background, the sample is acoustically moved out of the field of view by tuning the respective frequency.

3. Experiments and Results

3.1. Combined Experimental Setup

Our experimental platform is schematically shown in Fig. 1 **b**. The sample chambers and the acoustic device are mounted on a commercial inverted light microscope (Nikon ECLIPSE Ti2-E). The QPI measurement systems, DHM and Coded WFS, are installed on two separate observation ports, labeled image plane in Fig. 1 **a**.

In the DHM setting the sample is illuminated by a collimated beam from a fibre coupled diode laser (TOPTICA iBeam smart, λ = 640 nm). The light scattered by the sample is collected by an objective lens (Nikon CFI Apochromat LWD Lambda-S 40× NA 1.15, water immersion) and imaged onto either of the two output ports of the microscope. A home-built common path shearing interferometer based on [6] enables phase-stable DHM measurements with trans-illumination through the acoustofluidic device. We record off-axis interferograms on a camera (mvBlueFOX3-2071) to obtain quantitative information about the amplitude and the phase of the optical field.

In the Coded WFS case, we use a broadband white LED (Thorlabs MWWHL4) with a smooth spectrum (color temperature 3000K) for illumination. It is mounted on the microscope after tilting back the original illumination module. We used a lens to focus the LED illumination onto the sample, increasing the illumination throughput. For the operation of the Coded WFS, it is necessary to capture a single reference image. For static samples, we move the observation region, and with the acoustofluidic chip, we acoustically move the sample out of the field of view. Afterwards, we set the target observation region and capture images of static or moving objects. The Coded WFS consists of a random binary phase mask, positioned 1.43 mm in front of a monochromatic sensor (Thorlabs 1501M-USB-TE), replacing the protection cover glass [24] (see Supplement 1, Section 1 for details).

In order to create phase videos, we mount the acoustofluidic trapping device on the microscope stage to trap and rotate individual fixated HEK 293 cells.

3.2. Validation Experiments

To verify the QPI capabilities of our Coded WFS setup against the DHM, a 3D-printed cluster of artificial 'HeLa cells' was imaged. The fabrication was performed using a two-photon polymerization lithography system, which enables 3D printing of structures of variable height on top of microscopy slides [35]. Identical models of HeLa cells, manufactured using a polymer with a RI of 1.55 at 633 nm, are placed in different orientations to form a cluster, where the maximum designed height of each cell is $\approx$ 8.4 µm. The height map was converted to an OPD map (in µm) by taking the product $h(r)\Delta\eta$, where h is the height and $\Delta\eta = 0.038$ is the RI contrast, considering immersion of the model in Zeiss Immersol 518F (RI = 1.512 at 640 nm), and is referred to as Phantom Design in Fig. 2 **a**.

The fabricated cluster is correspondingly immersed in Immersol 518F prior to imaging. Fig. 2 **a** shows the retrieved phases of the phantom using DHM and Coded WFS. Figs. 2 **b** and **c** compare the cross-sections and the pixel-wise absolute differences, respectively, of the OPDs retrieved by the two techniques with the designed OPD map of the phantom. The results, in addition to validating Coded WFS, demonstrate that non-planar reference waves can be used for Coded WFS in this setting, providing advantages in system setup.

The disagreements between the measured and designed OPDs are explained partially by the limited accuracy of the fabrication process. Fabrication of variable-height structures using this method has been found to deviate from the ideal design maps due to anisotropic shrinkage and varying energy dose of the polymerization beam. The discrepancies can occur due to the shape of the structures and their positions within the printed field of view [35]. Therefore, we also expect variation in the OPD profiles of different cells in the phantom. Nonetheless, printed 3D phantoms replicating complex cells enable the quantitative comparison of different QPI systems and serve as an intermediary step before imaging real dynamic cells.

To improve the quality of the acquired OPDs, the following additional steps were taken. In DHM, we evaluate the complex field of the background (in the absence of the specimen), which is subtracted from the complex field of the object, ensuring the removal of tilts and artifacts in the background. For Coded WFS, the background is removed using a fit on the empty area of the phase map. To evaluate phase delay relative to the background (immersion), the average phase delay due to the immersion is subtracted.

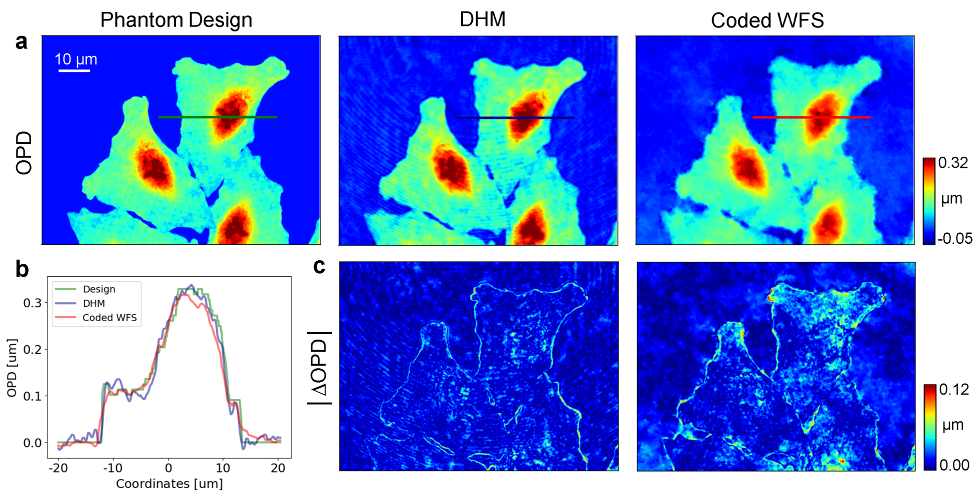

Fig. 2. **Performance validation using 3D-printed cluster of artificial HeLa cells.** **a** Designed OPD map of the HeLa cell cluster and measured OPD maps of the fabricated phantom using DHM and Coded-WFS. **b** Cross-sections of the OPDs in **a** relative to the immersion. **c** The pixel-wise absolute difference |ΔOPD| between the designed OPD map and the OPDs retrieved using DHM (left) and Coded-WFS (right).

3.3. Quantitative Phase and Amplitude Imaging of Rotating Cells

An inherent advantage of both DHM and Coded WFS over standard TIE-based curvature sensing techniques [9] and other computational microscopy methods is that only a single image of the specimen is required to recover the complex field at the image plane. For Coded WFS, the reference image without the specimen is required only once for a specific optical setup, which therefore does not hinder snapshot wavefront reconstruction.

We leverage the snapshot capabilities of DHM and Coded WFS to recover both the amplitudes and phases of cells at video rates $\approx$ 30 fps. A single HEK cell is trapped and actuated using the acoustofluidic trapping device described in Sect. 2.3 such that the cell rotates about an axis orthogonal to the imaging axis at $\approx 0.39\,\mathrm{rad\,s^{-1}}$. The exposure times for DHM and Coded WFS are 1.5 ms and 2 ms, respectively. The combined experimental setup, described in Sect. 3.1, enables video recording of the rotating cell in identical conditions for DHM and Coded WFS as it leaves the microscope, including the acoustofluidic chamber in the specimen plane, entirely unchanged except for the illumination unit. A two-observation port microscope allows for designated installation points for DHM and Coded WFS, and common-path shearing interferometry precludes changes within the microscope, ensuring separation of the two QPI systems. The same HEK cell rotating with the same periodicity [19] is therefore recorded successfully by each system in succession.

Fig. 3 shows agreement between the retrieved intensities and phases of selected frames of the cell at different angles of rotation using DHM and Coded WFS. Coded WFS retrieves clear brightfield intensity images while DHM suffers from diffraction artifacts. However, the spatial resolution of the DHM reconstructions is observed to be qualitatively better than Coded WFS. The differences are more perceptible in the video (see **Visualization 1**), where a side-by-side comparison of intensities and phases retrieved by both methods for one complete rotation (485 frames) is provided. Note that in both methods, the measurement rate is only limited by the camera hardware and not by the methods themselves. Therefore, due to the high temporal

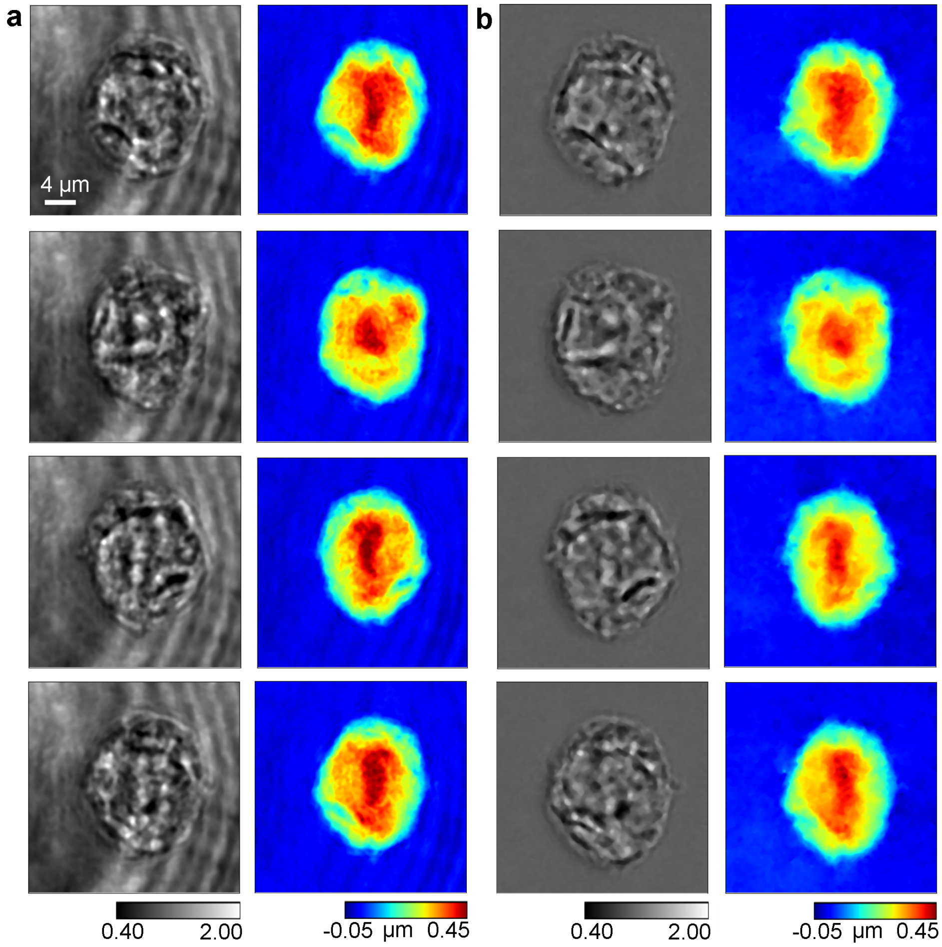

Fig. 3. **Video-rate (≈ 30 fps) QPI.** Quantitative reconstructions of intensity (left) and OPD (right) of corresponding frames using **a** DHM and **b** Coded WFS of a rotating HEK293 cell. The frames are chosen to reveal informative internal structures of the biological cell. Refer to the video (see **Visualization 1**) for one complete revolution of retrieved DHM and Coded WFS intensities and phases.

resolution of both DHM and Coded WFS, they are highly suitable to study dynamic specimens.

3.4. 3D Refractive Index Estimation

Traditional tomography setups use motorized mirror mounts to illuminate the specimen from different angles [21]. The finite angular extent of illumination leads to the missing cone problem, resulting in undesirable artifacts in the reconstruction. An alternative is to rotate the object by mechanical confinement and a motorized stage [14].

In comparison, the trapping and rotation of unknown objects using the acoustofluidic chamber is both contactless and allows unimpeded access to 360° of viewing angles about one (or more) object axis. However, because the object rotation is variable and unknown *a priori*, achieving an accurate tomographic reconstruction becomes more involved [23, 59].

In this work, our goal is to showcase the simplicity of the hardware setup required for

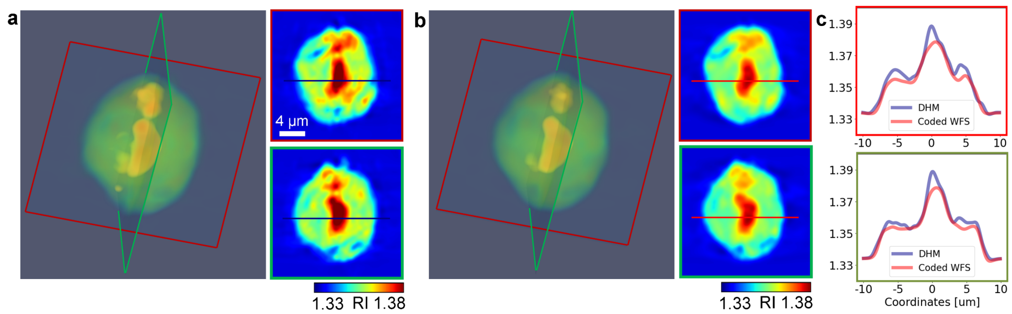

Fig. 4. **3D RI estimation.** 3D RI distribution (left) and two slices (right) corresponding to the planes in the 3D visualization of a HEK293 cell estimated using 360°-view OPDs retrieved by **a** DHM and **b** Coded WFS. **c** The red and green-bordered RI line profiles from the similarly bordered RI slices in **a** and **b**.

tomography with a Coded WFS scheme and to verify the estimated RI distribution by comparing it with DHM. For this purpose, we (i) retrieve the OPDs of the rotating HEK293 cell in Sect. 3.3 frame-by-frame, (ii) treat each OPD as a projection of the 3D RI distribution corresponding to a pose (angle of rotation corresponding to a reference), and (iii) make the following approximations for simplicity: First, since the precise pose information is not known, we approximate that the poses are distributed uniformly. Second, we apply a low-pass spatial filter to (a) mitigate specimen jitter and reduce perturbations between adjacent frames and (b) limit the frequency coverage of the data, enabling the use of the Fourier slice theorem (FST) for tomography.

We use the parallel geometry setting in the TIGRE toolbox [60] to simulate orthographic projection and the classical FDK algorithm [61] to estimate the 3D RI distribution of the HEK293 cell, which is shown in the left of Figs. 4 **a** and **b**. To inspect the quantitative RI, we examine two slices corresponding to the planes highlighted in the 3D visualization, where each point on the plane is an RI. The RI profiles corresponding to the lines on these slices are plotted in Fig. 4 **c**, which demonstrate that the retrieved RIs using DHM and Coded WFS are similar up to $|\mathrm{RI}| \lessapprox 0.01$. The dissimilarity follows from Fig. 3, where the Coded WFS underestimates OPDs compared to DHM. Smaller OPDs translate to smaller RIs. **Visualization 2** showcases the 360° view of the 3D RI distribution retrieved by the two methods. Even though no ground truth is available, the recovered RI range is in agreement with expected values [1].

While the approximations enable quick and easy 3D RI estimation, they reduce the fidelity of the tomographic reconstruction. Analyzing the spectrum of the OPD projections reveals that most of the energy is concentrated in the region where the Fourier diffraction theorem (FDT) arcs are approximately linear (see Supplement 1, Section 2 for details). This allows us to apply FST, provided we filter out the remaining spectrum. However, this approach comes at the cost of losing the ability to retrieve high-frequency structures. Moreover, the pose approximation is only accurate for objects with a spherical cross-section and a homogeneous density distribution. Considering a large frequency support without optimizing the poses first may introduce artifacts into the reconstruction.

4. Discussion and Conclusion

We have proposed and validated a novel approach to 3D RI tomography for individual cells: the acoustofluidic manipulation of the cell to enable the acquisition of 360 degree object poses in combination with video-rate QPI implemented via Coded WFS. Our approach lends itself to an implementation in an unmodified commercial microscope and, therefore has the potential to be widely applicable.

For validation, we have developed a combined experimental setup which enabled QPI using DHM and Coded WFS of phase specimens under identical experimental conditions. We have designed and fabricated a phantom replicating a cluster of cells, which enabled validation of phase accuracy of the Coded WFS method directly with the DHM.

The integration of the acoustofluidic chamber in the same setup allows for the levitation and rotation of biological cells. The retrieved intensities and phases of video-rate ($\approx$ 30 fps) data, recorded sequentially for DHM and Coded-WFS, demonstrate good agreement, validating Coded WFS as a suitable video-rate QPI method for our proposed technique. While DHM has been previously applied to 3D RI tomography [14], this is the first time, to our knowledge, that Coded WFS has been tested in this setting.

Our reported results rely on several restrictions and simplifying assumptions, namely i) a weak scattering regime, ii) a roughly spherical shape of the specimen to assume a uniform rotation over time, and iii) a limited maximum scattering angle caused by the specimen. Future work will address these challenges and allow for higher 3D spatial resolutions. To address i), multi-slice techniques in the forward model as e.g. in [55] would allow for stronger scattering to be successfully treated. A more complex specimen shape will cause more irregular rotations since the relevant forces apply varying amounts of torque at different object points. Pose estimation of the specimen may solve this problem and address issue ii). Finally, improved reconstruction algorithms can more fully account for the optical diffraction tomography geometry in the Fourier domain, contributing to improve issue iii).

Summarizing, we believe that our proposed approach carries significant potential for a simplified 3D RI tomography approach that may be well suited for a wide application.

Funding. This work was funded in part by the Austrian Science Fund (FWF) SFB 10.55776/F68 *Tomography Across the Scales*, project F6806-N36 Inverse Problems in Imaging of Trapped Particles and the German Research Foundation under DFG FOR 5336 *Learning to Sense* project IH 114/2-1. For open access purposes, the authors have applied a CC BY public copyright license to any author-accepted manuscript version arising from this submission.

Acknowledgement. Monika Ritsch-Marte and Ivo Ihrke would like to thank the Institute for Pure and Applied Mathematics (IPAM) at UCLA, where their current collaboration was initiated during the long program "Computational Microscopy". We thank Judith Hagenbuchner and Michael Ausserlechner (Medical University Innsbruck) for providing us with the fixated HEK 293 cells. We thank Armin Sailer (Institute for Experimental Physics, University of Innsbruck) for CNC-manufacturing the high-NA chip according to our design.

Disclosures. The authors declare no conflicts of interest.

Data availability. Data underlying the results presented in this paper are not publicly available at this time but may be obtained from the authors upon reasonable request.

Supplemental document. See Supplement 1 for supporting content.

References

1. P. Y. Liu, L. K. Chin, W. Ser, *et al.*, “Cell refractive index for cell biology and disease diagnosis: Past, present and future,” Lab on a Chip **16**, 634–644 (2016).
2. M. Habaza, M. Kirschbaum, C. Guernth-Marschner, *et al.*, “Rapid 3D refractive-index imaging of live cells in suspension without labeling using dielectrophoretic cell rotation,” Adv. Sci. **4**, 1600205 (2017).
3. S. Chowdhury, W. J. Eldridge, A. Wax, and J. Izatt, “Refractive index tomography with structured illumination,” Optica **4**, 537–545 (2017).
4. H. Hugonnet, H. Hugonnet, M. Lee, *et al.*, “Optimizing illumination in three-dimensional deconvolution microscopy for accurate refractive index tomography,” Opt. Express **29**, 6293–6301 (2021).
5. E. Cuche, P. Marquet, and C. Depeursinge, “Spatial filtering for zero-order and twin-image elimination in digital off-axis holography,” Appl. Opt. **39**, 4070–4075 (2000).
6. P. Girshovitz and N. T. Shaked, “Compact and portable low-coherence interferometer with off-axis geometry for quantitative phase microscopy and nanoscopy,” Opt. Express **21**, 5701–5714 (2013).

7. E. Sánchez-Ortiga, A. Doblas, G. Saavedra, *et al.*, "Off-axis digital holographic microscopy: practical design parameters for operating at diffraction limit," Appl. Opt. **53**, 2058–2066 (2014).
8. M. R. Teague, "Deterministic Phase Retrieval: A Green's Function Solution," J. Opt. Soc. Am. **73**, 1434–1441 (1983).
9. C. Zuo, J. Li, J. Sun, *et al.*, "Transport of Intensity Equation: a Tutorial," Opt. Lasers Eng. **135**, 106187 (2020).
10. P. F. Almoro, G. Pedrini, P. N. Gundu, *et al.*, "Phase microscopy of technical and biological samples through random phase modulation with a diffuser," Opt. Lett. **35**, 1028–1030 (2010).
11. Y. Park, C. Depeursinge, and G. Popescu, "Quantitative phase imaging in biomedicine," Nat. Photonics **12**, 578–589 (2018).
12. N. Goswami, M. A. Anastasio, and G. Popescu, "Quantitative phase imaging techniques for measuring scattering properties of cells and tissues: a review—part I," J. Biomed. Opt. **29**, S22713–S22713 (2024).
13. N. Goswami, M. A. Anastasio, and G. Popescu, "Quantitative phase imaging techniques for measuring scattering properties of cells and tissues: a review–part II," J. Biomed. Opt. **29**, S22714–S22714 (2024).
14. F. Charrière, A. Marian, F. Montfort, *et al.*, "Cell refractive index tomography by digital holographic microscopy," Opt. Lett. **31**, 178 (2006).
15. M. Habaza, B. Gilboa, Y. Roichman, and N. T. Shaked, "Tomographic phase microscopy with 180 rotation of live cells in suspension by holographic optical tweezers," Opt. Lett. **40**, 1881–1884 (2015).
16. K. Kim and Y. Park, "Tomographic active optical trapping of arbitrarily shaped objects by exploiting 3D refractive index maps," Nat. Commun. **8**, 15340 (2017).
17. T. Cacace, P. Memmolo, M. M. Villone, *et al.*, "Assembling and rotating erythrocyte aggregates by acoustofluidic pressure enabling full phase-contrast tomography," Lab on a Chip **19**, 3123–3132 (2019).
18. M. K. Løvmo, B. Pressl, G. Thalhammer, and M. Ritsch-Marte, "Controlled orientation and sustained rotation of biological samples in a sono-optical microfluidic device," Lab on a Chip **21**, 1563–1578 (2021).
19. M. K. Løvmo, S. Moser, G. Thalhammer-Thurner, and M. Ritsch-Marte, "Acoustofluidic trapping device for high-na multi-angle imaging," Front. Phys. **10**, 940115 (2022).
20. W. Choi, C. Fang-Yen, K. Badizadegan, *et al.*, "Tomographic phase microscopy," Nat. Methods **4**, 717–719 (2007).
21. Y. Sung, W. Choi, C. Fang-Yen, *et al.*, "Optical diffraction tomography for high resolution live cell imaging," Opt. Express **17**, 266–277 (2009).
22. X. Ma, W. Xiao, and F. Pan, "Optical tomographic reconstruction based on multi-slice wave propagation method," Opt. Express **25**, 22595–22607 (2017).
23. S. Moser, M. Kvåle løvmo, F. Strasser, *et al.*, "Optical tomography reconstructing 3D motion and structure of multiple-scattering samples under rotational actuation," Optica **12**, 594–603 (2025).
24. C. Wang, Q. Fu, X. Dun, and W. Heidrich, "Quantitative phase and intensity microscopy using snapshot white light wavefront sensing," Sci. Reports **9**, 13795 (2019).
25. E. Cuche, P. Marquet, and C. Depeursinge, "Simultaneous amplitude-contrast and quantitative phase-contrast microscopy by numerical reconstruction of fresnel off-axis holograms," Appl. Opt. **38**, 6994–7001 (1999).
26. P. Marquet, B. Rappaz, P. J. Magistretti, *et al.*, "Digital holographic microscopy: a noninvasive contrast imaging technique allowing quantitative visualization of living cells with subwavelength axial accuracy," Opt. Lett. **30**, 468–470 (2005).
27. D. Gabor, "A new microscopic principle," Nature **161**, 777–778 (1948).
28. D. Gabor, "Microscopy by reconstructed wave-fronts," Proc. Royal Soc. London. Ser. A. Math. Phys. Sci. **197**, 454–487 (1949).
29. J. Goodman and R. Lawrence, "Digital image formation from electronically detected holograms," Appl. Phys. Lett. **11**, 77–79 (1967).
30. T. Zhang and I. Yamaguchi, "Three-dimensional microscopy with phase-shifting digital holography," Opt. Lett. **23**, 1221–1223 (1998).
31. K. M. Eder, A. Marzi, Á. Barroso, *et al.*, "Label-free digital holographic microscopy for in vitro cytotoxic effect quantification of organic nanoparticles," Cells **11**, 644 (2022).
32. B. Javidi, A. Carnicer, A. Anand, *et al.*, "Roadmap on digital holography," Opt. Express **29**, 35078–35118 (2021).
33. J. M. Wittkopp, T. C. Khoo, S. Carney, *et al.*, "Comparative phase imaging of live cells by digital holographic microscopy and transport of intensity equation methods," Opt. Express **28**, 6123–6133 (2020).
34. S. Obando-Vásquez, M. J. Lopera, R. Restrepo, and C. Trujillo, "Comparative analysis of digital holographic microscopy and digital lensless holographic microscopy for quantitative phase imaging," Opt. Continuum **3**, 309–323 (2024).
35. S. Desissaire, M. Ziemczonok, T. Cantat-Moltrecht, *et al.*, "Bio-inspired 3d-printed phantom: Encoding cellular heterogeneity for characterization of quantitative phase imaging," Measurement **247**, 116765 (2025).
36. D. Malacara-Hernández and D. Malacara-Doblado, "What is a Hartmann test?" Appl. Opt. **54**, 2296–2301 (2015).
37. R. V. Shack and B. C. Platt, "Production and use of a lenticular Hartmann screen." J. Opt. Soc. Am. A **61**, 656 (1971).
38. L. K. Saddlemyer, G. Herriot, J.-P. Veran, and J. M. Fletcher, "Design aspects of the reconstructor for the Gemini adaptive optics system (Altair)," in *Adaptive Optical System Technologies,* vol. 3353 (SPIE, 1998), pp. 150–159.
39. W. Harm, C. Roider, A. Jesacher, *et al.*, "Lensless imaging through thin diffusive media," Opt. Express **22**, 22146–22156 (2014).
40. S. Bernet, W. Harm, A. Jesacher, and M. Ritsch-Marte, "Lensless digital holography with diffuse illumination

through a pseudo-random phase mask," Opt. Express **19**, 25113–25124 (2011).
41. P. Berto, H. Rigneault, and M. Guillon, "Wavefront sensing with a thin diffuser," Opt. Lett. **42**, 5117–5120 (2017).
42. C. Wang, X. Dun, Q. Fu, and W. Heidrich, "Ultra-high resolution coded wavefront sensor," Opt. Express **25**, 13736–13746 (2017).
43. S. Feng, C. Kane, P. A. Lee, and A. D. Stone, "Correlations and fluctuations of coherent wave transmission through disordered media," Phys. Rev. Lett. **61**, 834–837 (1988).
44. I. Freund, M. Rosenbluh, and S. Feng, "Memory effects in propagation of optical waves through disordered media," Phys. Rev. Lett. **61**, 2328–2331 (1988).
45. H. Penketh and J. Bertolotti, "Imaging through scattering media by exploiting the optical memory effect: a tutorial," J. Physics: Photonics (2024).
46. B. K. Horn and B. G. Schunck, "Determining optical flow," Artif. Intell. **17**, 185–203 (1981).
47. E. Wolf, "Three-dimensional structure determination of semi-transparent objects from holographic data," Opt. Commun. **1**, 153–156 (1969).
48. R. Dändliker and K. Weiss, "Reconstruction of the three-dimensional refractive index from scattered waves," Opt. Commun. **1**, 323–328 (1970).
49. A. C. Kak and M. Slaney, *Principles of Computerized Tomographic Imaging* (SIAM, 2001).
50. P. Müller, M. Schürmann, and J. Guck, "The theory of diffraction tomography," (2016).
51. A. Barty, K. Nugent, A. Roberts, and D. Paganin, "Quantitative phase tomography," Opt. Commun. **175**, 329–336 (2000).
52. U. S. Kamilov, I. N. Papadopoulos, M. H. Shoreh, *et al.*, "Learning approach to optical tomography," Optica **2**, 517 (2015).
53. J. Lim, A. B. Ayoub, E. E. Antoine, and D. Psaltis, "High-fidelity optical diffraction tomography of multiple scattering samples," Light. Sci. & Appl. **8** (2019).
54. M. Chen, D. Ren, H.-Y. Liu, *et al.*, "Multi-layer born multiple-scattering model for 3d phase microscopy," Optica **7**, 394 (2020).
55. S. Moser, A. Jesacher, and M. Ritsch-Marte, "Efficient and accurate intensity diffraction tomography of multiple-scattering samples," Opt. Express **31**, 18274–18289 (2023).
56. J. W. Goodman, *Introduction to Fourier optics* (Roberts and Company publishers, 2005).
57. J. Bühl, H. Babovsky, A. Kiessling, and R. Kowarschik, "Digital synthesis of multiple off-axis holograms with overlapping fourier spectra," Opt. Commun. **283**, 3631–3638 (2010).
58. L. Huang, M. Idir, C. Zuo, *et al.*, "Comparison of two-dimensional integration methods for shape reconstruction from gradient data," Opt. Lasers Eng. **64**, 1–11 (2015).
59. M. Kvåle Løvmo, S. Deng, S. Moser, *et al.*, "Ultrasound-induced reorientation for multi-angle optical coherence tomography," Nat. Commun. **15**, 2391 (2024).
60. A. Biguri, M. Dosanjh, S. Hancock, and M. Soleimani, "TIGRE: a MATLAB-GPU toolbox for CBCT image reconstruction," Biomed. Phys. & Eng. Express **2**, 055010 (2016).
61. L. A. Feldkamp, L. C. Davis, and J. W. Kress, "Practical cone-beam algorithm," J. Opt. Soc. Am. A **1**, 612–619 (1984).